Nano Research

Open Access

Research Article

Dental curing light-triggered on-target CO release from NHC-Fe complex for cancer immunotherapy

Wu-Yin Wang[1,§], Haozhe Dong[2,§], En-Li Yang[1], Xiaoqian He[2], Zhiqiang Zhang[2], Qing Wang[1], Nian Chen[2], Hong Yi[2] ✉, Aiwen Lei[2,3] ✉, and Zhi-Jun Sun[1] ✉

[1] *State Key Laboratory of Oral & Maxillofacial Reconstruction and Regeneration, Key Laboratory of Oral Biomedicine, Ministry of Education, Hubei Key Laboratory of Stomatology, School & Hospital of Stomatology, Frontier Science Center for Immunology and Metabolism, Taikang Center for Life and Medical Sciences, Wuhan University, Wuhan 430079, China*
[2] *Institute for Advanced Studies (IAS), Wuhan University, Wuhan 430072, China*
[3] *College of Chemistry and Molecular Sciences, Wuhan University, Wuhan 430072, China*
§ *Wu-Yin Wang and Haozhe Dong contributed equally to this work.*

Cite this article: *Nano Research*, **2026**, *19*, 94908830. https://doi.org/10.26599/NR.2026.94908830

ABSTRACT: Malignant tumors remain a leading cause of premature death worldwide, with disproportionately increasing burdens in resource-limited regions. Although immune checkpoint blockade (ICB) has emerged as a transformative cancer therapy, its efficacy is often limited by the immunosuppressive tumor microenvironment (TME). Leveraging iron as the most abundant bioactive transition metal in Earth's crust, we report **F-Fe**, a complex IV-targeted carbon monoxide-releasing molecule (CORM) that is activated by a clinically approved dental light-curing unit to induce pyroptosis for reprogramming the TME. We developed a bioinspired delivery system named GLEAM to facilitate clinical applications that adhere to tissue surfaces while channeling light into deeper tissue for on-target CO release, simultaneously providing real-time visual feedback for treatment monitoring. Murine oral and breast cancer models validated the therapeutic efficacy, showing significant tumor suppression and TME remodeling. When combined with anti-PD-1 antibody (aPD-1) therapy, it markedly suppressed metastasis, prevented recurrence, and prolonged survival. Our findings suggest that Fe-based small molecules with biomimetic delivery can leverage dental light to boost ICB efficacy, offering a sustainable and translational approach to tumor treatment.

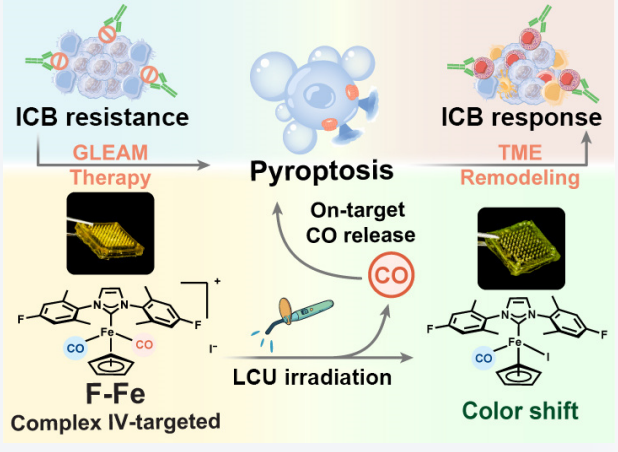

KEYWORDS: Fe-N-heterocyclic carbene (NHC) complexes, carbon monoxide-releasing molecules, biomimetic delivery, immunotherapy, mitochondrial complex IV targeting

1 Introduction

Malignant tumors remain a major cause of premature death globally, with incidence and mortality increasing especially swiftly in areas facing resource constraints [1, 2]. Following the surgery, chemotherapy, and radiotherapy, cancer immunotherapy exemplified by immune checkpoint blockade (ICB) has transformed the treatment landscape by harnessing the host immune system to eliminate malignant cells, marking a significant advancement in oncology [3]. However, the majority of patients do not experience durable benefit from ICB, largely due to primary or acquired resistance mechanisms driven by the immunosuppressive tumor microenvironment (TME) [4].

Once known mainly for its toxicity, carbon monoxide (CO) is now explored as an anticancer agent for its ability to modulate cellular signaling pathways and remodel the TME [5]. Photoactivation of CORMs provides a way to generate high concentrations of CO specifically within tumors. Such localized CO delivery can inhibit mitochondrial complex IV (cytochrome *c*

Received: March 11, 2026; **Revised:** May 8, 2026
Accepted: May 11, 2026

✉Address correspondence to Hong Yi, hong.yi@whu.edu.cn; Aiwen Lei, aiwenlei@whu.edu.cn; Zhi-Jun Sun, sunzj@whu.edu.cn

oxidase (C*c*O)) [5] and directly kill cancer cells, while also inducing immunogenic cell death [6], enhancing antitumor T cell function [7], and promoting M1-like macrophage polarization [8]. These effects collectively convert the TME into an immunologically "hot" state, making it more responsive to ICB therapy. Because complex IV is central to CO's cytotoxic effects, rationally designing a carbon monoxide-releasing molecule (CORM) with selective complex IV targeting could amplify these therapeutic benefits (Fig. 1).

Transition metal-based agents remain a cornerstone of oncology, exemplified by cisplatin's enduring clinical value, while many emerging therapeutics exploit trace amounts of transition elements [9, 10]. Seeking an accessible and sustainable strategy, iron (Fe) shows application potential, which is the most abundant transition metal in Earth's crust and an essential bioelement [11, 12], as the core for CORMs [13, 14]. As a 3D metal, the flexible electronic structure of Fe enables diverse coordination with CO ligands [15, 16]. And the chemical property and photophysical behavior of Fe-complexes have sufficient margin for adjustment through ligand engineering [17–19], benefiting to enhance potential biological activity. *N*-heterocyclic carbenes (NHCs) provide an ideal scaffold, offering modifiable heterocycles and wing groups to fine-tune molecular geometry and electronics [20], thereby creating abundant sites for optimizing photochemical characteristics and pharmacodynamic properties, with the potential to confer enhanced biological targeting [21–23]. Their well-characterized coordination chemistry, combined with the pronounced photoinduced CO release observed in NHC-Fe complexes via high-energy photon-triggered ligand exchange [24], makes them strong candidates for clinically relevant photoactivation after further modification. Leveraging these features, we envisioned NHC-Fe CORMs activatable by clinically approved dental light-curing units (LCU, ~ 460 nm) [25] for targeted CO delivery and translational potential.

To facilitate clinical application, effective delivery strategies must ensure both compound accumulation and sufficient light penetration into tumors. Microneedle patches offer painless, minimally invasive administration for cancer therapy and TME modulation [26–28], with tunable geometry, multilayer designs, and bioinspired features that enhance tissue retention [29], control drug release [30], and even deliver high-energy photons [31]. Inspired by *Octopus vulgaris*, whose sharp beak and suction cups enable a firm grip [32], we developed the GLEAM system, integrating a photon-guiding core with puncture and adhesive structures. The soluble tip, analogous to the beak, encapsulates the NHC-Fe-based CORM (**F-Fe**) that targets mitochondrial complex IV and undergoes light-triggered CO release under LCU irradiation. Upon illumination, the cone guides light deep into tissue, inducing on-target CO release that disrupts cancer cell respiration and triggers gasdermin E (GSDME)-dependent pyroptosis. A distinct color change provides real-time visual feedback. This process reprograms the TME, activates systemic immunity, and establishes durable immune memory, markedly enhancing anti-PD-1 antibody (aPD-1) therapy, prolonging survival, and reducing recurrence and metastasis in preclinical models (Fig. 1).

2 Experimental

2.1 General information

All reactions to synthesize Fe complexes were carried out in a glove box (Vigor) under an argon atmosphere. Ligands were placed in a vacuum drying oven at 50 °C overnight before metal-coordinating procedures. All glassware was oven dried at 80 °C for several hours and cooled down under vacuum. Unless otherwise noted, all substrates were obtained from commercial suppliers and used without further purification. Thin-layer chromatography (TLC) employed glass 0.25 mm silica gel plates. Flash chromatography columns were packed with 200–300 mesh silica gel in petroleum (bp. 60–90 °C).

2.2 Surface plasmon resonance (SPR)

Surface plasmon resonance experiments were conducted using a Biacore T200 instrument (GE Life Sciences). Cytochrome *c* oxidase from bovine heart (Cat. C5499) was immobilized onto a Series S Sensor Chip CM7 (Cat. 28953828, Cytiva) via standard amine coupling. Varying concentrations of the molecules were injected over the surface at a constant flow rate. Association and dissociation phases were recorded in real time. The sensorgrams were fitted to a 1:1 Langmuir binding model using Biacore Evaluation Software to calculate kinetic parameters and the equilibrium dissociation constant (K_d). Hemoglobin (Hb) from bovine blood (Cat. abs47047819, Absin) was immobilized on the sensor chip using the same method to detect CO release. PBS solutions without **F-Fe**, as well as **F-Fe** samples before and after LCU irradiation, were sequentially injected over the surface, and the resulting response signals were recorded.

2.3 Mitochondrial complex IV (C*c*O) activity assay

Mitochondria were isolated from 4T1 cells, and C*c*O solution was prepared using the reagents provided in the Mitochondrial Complex IV/Cytochrome *c* Oxidase Activity Assay Kit (Cat. BC0940, Solarbio). Different concentrations of **F-Fe** were added to the reaction system, followed by either LCU illumination or dark incubation on ice. A ultraviolet–visible (UV–Vis) spectrophotometer (UV-3600, Shimadzu) was used to continuously record absorbance at 550 nm for 70 s, and enzyme activity was quantified accordingly.

2.4 Cellular culture

The murine breast cancer cell line 4T1 (Cat. TCM-C705), human tongue squamous cell carcinoma CAL 27 (Cat. TCH-C148), human breast ductal carcinoma HCC1937 (Cat. TCH-C181), human colorectal adenocarcinoma HCT-15 (Cat. TCH-C186), and human breast adenocarcinoma MCF7 (Cat. TCH-C247) were purchased from Hycyte. The murine head and neck squamous cell carcinoma SCC7 was kindly provided by Prof. Qianming Chen (West China School and Hospital of Stomatology, Sichuan University, Chengdu, China). The 4MOSC1 cells were generously gifted by J. Silvio Gutkind (University of California, San Diego, USA) under a material transfer agreement (SD2017-202). 4T1, HCC1937, and HCT-15 cells were cultured in Roswell Park Memorial Institute 1640 medium (RPMI-1640) supplemented with 10% (v/v) fetal bovine serum (FBS) and 1% (v/v) Penicillin/Streptomycin (P/S). SCC7 and CAL 27 cells were maintained in high-glucose Dulbecco's modified Eagle medium (DMEM) with 10% FBS and 1% P/S. RPMI-1640 medium, DMEM medium, FBS, and Penicillin/Streptomycin were obtained from Gibco. MCF7 cells were cultured in MEM medium supplemented with 10% FBS, 1% GlutaMAX, 1% non-essential amino acids (NEAA), 1% sodium pyruvate, 10 μg·mL^{-1} recombinant human insulin, and 1% P/S (Cat.

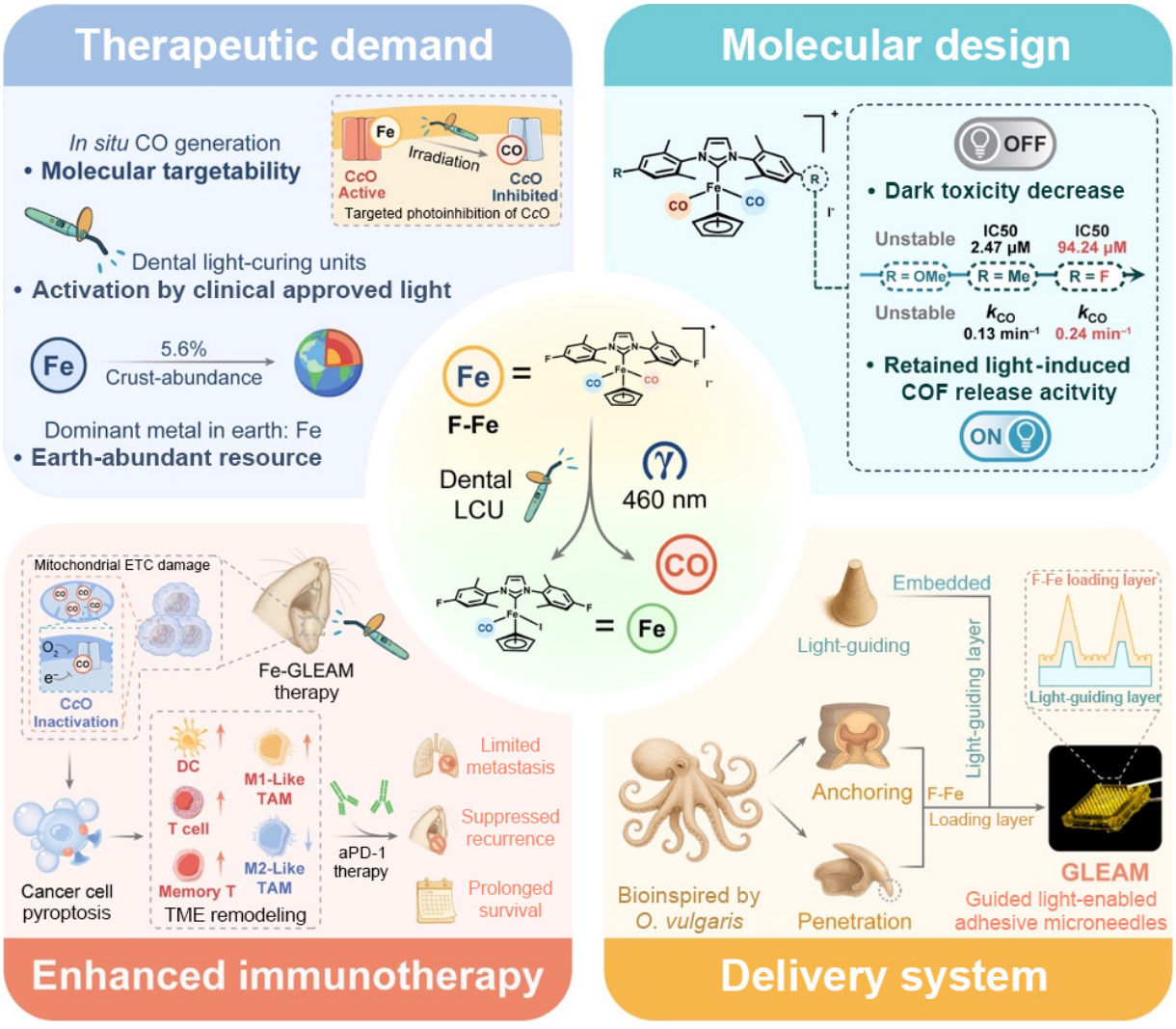

Figure 1 Schematics of complex IV-targeted, clinical photoactivatable Fe-CORMs and the bioinspired multifunctional delivery system GLEAM for enhancing ICB therapy. The Fe-based CORM **F-Fe** was designed via ligand engineering, targets mitochondrial complex IV with high affinity and releases CO upon activation by clinically approved dental LCUs, with a visible yellow-to-green color change enabling real-time monitoring. To enable clinical translation of **F-Fe**, the guided light-enabled adhesive microneedles (GLEAM) system, inspired by *O. vulgaris* beak and suction-cup structures, integrates a soluble **F-Fe**-loaded tip with an optically transparent, light-guiding base to deliver photons into deeper tissue. This approach achieves on-target CO release, induces pyroptosis, reprograms the TME, and synergizes with aPD-1 therapy to suppress tumor growth, metastasis, and recurrence, prolonging survival in murine models, representing a sustainable approach to therapeutic development by harnessing Earth's most abundant transition metal.

TCH-G247, hycyte). 4MOSC1 cells were maintained in Keratinocyte-SFM medium (K-SFM, Cat. 10744019, Gibco) supplemented with 1% P/S, 5 ng·mL^{-1} mouse epidermal growth factor (EGF, Cat. PMG8041, Invitrogen), and 5 × 10^{-11} M cholera toxin (Cat. 8052, Sigma). All cells were cultured at 37 °C in a humidified incubator containing 95% air and 5% CO_2.

2.5 Animal experiment

Animal experiments were reviewed and approved by the Ethics Committee for Experimental Animals of the School and Hospital of Stomatology, Wuhan University (approval number: S07923030F). All procedures were conducted in accordance with the Regulations for the Administration of Affairs Concerning Experimental Animals, issued by the State Council of the People's Republic of China. All animals were housed under specific pathogen-free (SPF) conditions at a controlled temperature of approximately 22 °C and relative humidity of ~ 50%, with a 12 h light/dark cycle.

For the orthotopic 4MOSC1 oral cancer model, female C57BL/6 mice aged 6–8 weeks were inoculated with 1 × 10^6 viable 4MOSC1 cells in 30 μL of PBS directly into the tongue. The first intervention was initiated 5 days post-inoculation. To ensure animal welfare, all groups involved in oral cancer experiments were provided with a complete nutritional gel supplement (Cat. SL0043, Shulaibao (Wuhan) Biotechnology Co., Ltd.) in addition to standard husbandry. For the subcutaneous 4T1 breast cancer model, female BALB/c mice aged 6–8 weeks received a subcutaneous injection of 1 × 10^6 4T1 cells suspended in 100 μL of PBS into the right flank. Treatment began on day 7 after tumor implantation.

For Fe-GLEAM treatment, mice were anesthetized with isoflurane, and the Fe-GLEAM patch was applied to the tumor site. After 10 min of contact, light irradiation was performed using the previously described LCU for approximately 1 min, until the patch turned completely green indicating complete activation. The remaining GLEAM was then discarded. For ICB therapy,

InVivoMAb anti-mouse programmed cell death protein 1 (PD-1) (CD279, Cat. BE0146, Bio X Cell) was administered intraperitoneally at a dose of 10 mg·kg^{-1}.

For bioluminescence imaging, mice were injected with luciferase-transgenic 4T1 (4T1-Luc) cells at the same dose as described above. Prior to imaging, D-luciferin (150 mg·kg^{-1}) was administered intraperitoneally. Bioluminescence signals were then acquired using an IVIS Spectrum Imaging System (PerkinElmer) and analyzed with Living Image software (PerkinElmer).

2.6 Phototoxicity and dark toxicity assay of molecules

Various cell lines were seeded into 24-well plates at a density of approximately 2 × 10^4 cells per well. After reaching the logarithmic growth phase, cells were treated with the test compound solutions and incubated at 37 °C for 15 min. For the light treatment group, samples were irradiated using a dental LCU (V200, Veirun) for 1 min. After 24 h, cell viability was assessed using a CCK-8 staining kit (Cat. BS350C, Biosharp). All cell experiments involving light irradiation and their corresponding controls were conducted in phenol red-free RPMI-1640 medium (PM150120, Pricella) and DMEM (PM150223, Pricella).

2.7 Oxygen consumption rate analysis

Oxygen consumption rate (OCR) of cancer cells was measured using Seahorse XF 24 Analyzer (Seahorse Biosciences) with Seahorse XF Cell Mito Stress Test Kit (Cat. 103015-100, Seahorse Biosciences). Basal measurements were collected 3 times, followed by 3 measurements after addition of oligomycin (final concentration 1.5 μM), followed by 3 measurements after addition of carbonyl cyanide 4-(trifluoromethoxy)phenylhydrazone (FCCP) (final concentration 2.5 μM), followed by 3 measurements after addition of antimycin A and rotenone (final concentration 0.5 μM).

2.8 Western blotting

Cells were lysed using Radioimmunoprecipitation assay (RIPA) lysis buffer supplemented with phenylmethanesulfonyl fluoride (PMSF; Cat. ST506, Beyotime). Equal amounts of protein were subjected to sodium dodecyl sulfate–polyacrylamide gel electrophoresis (SDS-PAGE) for size-based separation (Cat. ET15412Gel, ACE), followed by transfer onto polyvinylidene difluoride (PVDF) membranes. After blocking, membranes were incubated overnight at 4 °C with primary antibodies, then washed and probed with horseradish peroxidase (HRP)-conjugated goat anti-rabbit IgG (Cat. SA00001-2, Proteintech). Signal detection was performed using an enhanced chemiluminescence (ECL) kit (Cat. BL520B, Biosharp) and visualized with the Odyssey imaging system (LI-COR Biosciences). Quantification was conducted using Image Studio software (Version 5.2.5). Membranes were stripped using stripping buffer (Cat. CW0056M, CWBIO), re-blocked, and re-probed with the next antibody. This process was repeated until all targets were assessed. The primary antibodies used in this study are as follows: anti-DFNA5/GSDME-N-terminal (Cat. ab215191, 1:1000, Abcam); anti-cleaved caspase-3 (Cat. 9664, 1:1000, Cell Signaling Technology); and HRP-conjugated beta-actin monoclonal antibody (Cat. HRP-60008, 1:10000, Proteintech). All experiments were performed in at least three independent biological replicates.

2.9 LDH and adenosine triphosphate (ATP) release assay

Cells were seeded into 24-well plates at a density of 2 × 10^4 cells per well. After 24 h, the medium was replaced with phenol red-free medium containing **F-Fe** or an equal volume of PBS. Cells were incubated for 15 min, followed by LCU irradiation or no irradiation as a control. After an additional 12 h incubation, the supernatants were collected and centrifuged at 10,000*g* to remove cellular debris. The LDH Cytotoxicity Assay Kit (Cat. C0016, Beyotime) and the Enhanced ATP Assay Kit (Cat. S0027, Beyotime) were used to quantify the levels of LDH and ATP, respectively, in the supernatants. The data were normalized and visualized as a heatmap.

2.10 Construction and characterization of GLEAM

Microneedle master molds were fabricated using a high-resolution 3D printer (nanoArch S140, BMF Precision Tech Inc.) with HTL resin. Corresponding negative molds were then replicated using polydimethylsiloxane (PDMS, SYLGARD 184 Silicone Elastomer Kit, Dow Chemical). Polyvinyl alcohol (PVA, Cat. EFL-PVA-001, EFL) solution was cast into the PDMS mold to form the light-guiding cone and base layer, while sodium hyaluronate (Cat. EFL-HA-150K, EFL) solution was applied to the outer surface to construct the adhesive outer structure and the needle tip. Quality control was conducted via optical microscopy. Surface morphology was examined by scanning electron microscopy (SEM, TESCAN CLARA). The optical transmittance of the PVA substrate was measured using UV–Vis spectroscopy (UV-3600, Shimadzu). Mechanical properties were evaluated using a digital force measuring instrument (SF-5, Aipli).

2.11 Immunofluorescence and multiplex immunohistochemical analysis

Cells were seeded at a density of 2 × 10^4 cells per well in 24-well plates and incubated for 24 h. After the designated treatments, cells were fixed with 4% paraformaldehyde. Primary antibody used was anti-high mobility group box 1 (HMGB1) (Cat. 6893, CST). Secondary antibody was DyLight 488 goat anti-rabbit IgG (Cat. A23220, Abbkine). Nuclei were counterstained using Antifade Mounting Medium with 4',6-diamidino-2-phenylindole (DAPI) (Cat. P0131, Beyotime). For tissue samples, 4 μm-thick paraffin sections were prepared following fixation with 4% paraformaldehyde. Multiplex immunostaining was performed using the OPAL 6-Plex Manual Detection Kit (Cat. NEL811001KT, Akoya Biosciences) according to the manufacturer's instructions. The following primary antibodies were used: CD8 (Cat. 98941), granzyme B (GZMB) (Cat. 46890), F4/80 (Cat. 70076), CD86 (Cat. 19589), and mannose receptor C-type 1 (MRC1)/CD206 (Cat. 24595), all purchased from Cell Signaling Technology (CST). Slides were imaged using the Vectra 3 Automated Quantitative Pathology Imaging System (PerkinElmer).

2.12 Flow cytometry

Tumor tissues, tumor-draining lymph nodes (TDLNs), and spleens were harvested from mice and processed into single-cell suspensions. Cells were subsequently stained in 96-well U-bottom plates according to the manufacturers' instructions. The antibodies used for flow cytometry included the following: anti-CD62L-allophycocyanin (APC) (MEL-14), anti-MHCII-PC7 (M5/114.15.2), and anti-F4/80-PE-Cyanine7 (BM8), all purchased from eBioscience; anti-CD45-APC-Cy7 (2D1), anti-CD3-fluorescein isothiocyanate (FITC) (17A2), anti-CD8-PC5.5 (53-6.7), anti-CD11b-FITC (M1/70), anti-Ly6G-phycoerythrin (PE) (1A8),

and anti-CD206-APC (C068C2), all from BioLegend; anti-CD4-eFluor450 (RM4-5), anti-CD44-PE (IM7), anti-CD11c-FITC (N418), anti-CD80-PE (16-10A1), anti-CD86-APC (GL1), and anti-Ly6C-APC (HK1.4), all from Invitrogen; anti-CD45-APC-cyanine 7 (Cy7) (2D1). A Fixable Viability Dye eFluor 506 (Cat. 65-0866-14, eBioscience) was used to exclude dead cells. Flow cytometric analysis was performed on a CytoFLEX LX Flow Cytometer (Beckman), and data were analyzed using CytoExpert (v. 2.3, Beckman Coulter) and FlowJo (v.10.8.1, FlowJo LLC) software.

2.13 Statistical analysis

All data are presented as mean ± standard error of mean (s.e.m). Comparisons between two groups were performed using a two-tailed Student's *t*-test, while comparisons among multiple groups were analyzed by one-way ANOVA followed by Tukey's multiple comparisons test. A P value < 0.05 was considered statistically significant and is indicated in the figures. Survival curves were analyzed using the log-rank (Mantel-Cox) test. Data analysis was performed using Excel 2019 (v.16.78, Microsoft) and GraphPad Prism (v.10.4.1, GraphPad Software).

3 Results and discussion

3.1 Molecular design of complex IV-targeted NHC-Fe CORMs

Motivated by reports that half-sandwich NHC-Fe complexes undergo photoinduced CO release, we initiated synthesis of **Me-Fe** by reacting $CpFe(CO)_2I$ with NHC ligand under dark conditions according to the literature (Fig. 2(a)) [33]. To confirm the CO release ability under dental LCU, UV–Vis spectra revealed that **Me-Fe** had absorption band at 360 nm and weak absorption at 460 nm (Fig. S17 in the in the Electronic Supplementary Material (ESM)), which markedly changed after 5 min of 460 nm light emitting diode (LED) exposure, with new bands at 455 and 660 nm (Fig. 2(b)), indicating light-induced structural changes in the molecule. However, **Me-Fe** exhibited pronounced dark toxicity *in vitro* without light irradiation, rendering it unsuitable for direct therapeutic application (Fig. 2(c)). Limited proteolysis-coupled mass spectrometry (LiP-MS) [34] showed that **Me-Fe** exhibits promiscuous interactions with thousands of proteins. Gene Ontology (GO) functional annotation further revealed that fundamental cellular processes, metabolism, and regulatory pathways proteins with catalytic, regulatory, and structural activities may be functionally impaired by **Me-Fe**, collectively accounting for its severe dark toxicity (Fig. 2(e) and Fig. S13 in the ESM).

Notably, among these potential targets we identified the mitochondrial complex IV fragment COX6a1 (Fig. S14 in the ESM). Since complex IV is the primary site through which CO disturbs cellular respiration [5], this finding suggests that **Me-Fe** could serve as a lead for designing CORMs with on-target activation under dental LCU irradiation, thereby enhancing tumor cell killing efficacy. Guided by the established influence of substituent electronics on pharmacodynamics, we retained the **Me-Fe** scaffold and modified its NHC ligand wing group by replacing the phenyl methyl substituent with either methoxy (**OMe-Fe**) or fluorine (**F-Fe**). The structures were confirmed by single-crystal X-ray diffraction (SC-XRD), high-resolution mass spectroscopy (HRMS), and nuclear magnetic resonance (NMR) spectroscopy (Fig. 2(d), Figs. S2–S12 in the ESM, and Table S1 in the ESM). UV–Vis absorption spectra and ^{19}F NMR spectra demonstrated that **F-Fe** acquired the light-induced structural change upon 460 nm light irradiation (Fig. 2(c) and Fig. S25 in the ESM). However, methoxy substitution rendered the complex air-sensitive or light-induced dissociation process, which is unsuitable for drug development (Fig. S18 in the ESM). Meanwhile, replacing the methyl group in **Me-Fe** with its bioisostere fluorine markedly reduced dark toxicity (Fig. 2(c)), making **F-Fe** suitable for subsequent studies. LiP-MS analysis revealed that the introduction of the fluorine substituent substantially reduced the number of potential protein targets. The resulting decrease in non-specific binding suggests lower off-target effects, with minimal interference on enzymes, regulatory proteins, and structural proteins, which accounts for the observed reduction in cellular dark toxicity (Fig. 2(e) and Fig. S15 in the ESM). Simultaneously, SPR analysis confirmed that **F-Fe** retained the desired strong binding affinity for complex IV, with kinetic fitting yielding a dissociation constant (K_d) of 9.334×10^{-6} M (Fig. 2(f)), demonstrating that the introduction of the fluorine atom effectively enhances the molecule's targeting affinity compared to the **Me-Fe** structure (Fig. S16 in the ESM).

To directly demonstrate CO release process after irradiation, we employed Hb as a biomolecular probe, based on the principle that Hb normally binds O_2 but, in the presence of CO, rapidly forms CO-Hb accompanied by a redshift of its UV–Vis absorption peak [35]. We reproduced this phenomenon by introducing CO into an O_2-saturated Hb solution as a standard control (Fig. 2(g)). When **F-Fe** was added to an O_2-Hb solution and irradiated with a 460 nm LED, the low-energy doublet absorption peak of O_2-Hb underwent an obvious redshift, consistent with the phenomenon induced by CO, whereas no such redshift occurred in the absence of light. Besides, SPR analysis corroborated that the observed redshift originated from CO release. On the chip with immobilized Hb, **F-Fe** showed only very weak and reversible binding in the dark, which rapidly dissociated upon washing. In contrast, irradiation induced Hb capture of a substantial fraction of tightly bound molecules that resisted elution, consistent with the slow dissociation kinetics characteristic of the CO-Hb complex (Fig. S22 in the ESM). Combined with gas chromatography (GC) analysis (Fig. S23 in the ESM), the result provided direct evidence of photoinduced CO release behavior of **F-Fe**.

Although the precursor molecule $CpFe(CO)_2I$ also exhibited considerable absorption at 460 nm (Fig. S19 in the ESM), it did not display similar photo-responsive behavior upon irradiation, failing to trigger CO release and lacking anti-tumor efficacy under LCU illumination (Fig. S28 in the ESM). Density functional theory (DFT) calculations show that CO dissociation is thermodynamically unfavorable in the absence of an NHC ligand. With the assistance of the NHC ligand, CO release essentially converts to the ligand exchange process, making it thermodynamically feasible (Fig. 3(a)). The kinetics of CO release were further monitored using *in situ* infrared spectroscope (Figs. 3(b) and 3(c)). Despite the differing electronic effects of the ligand substituents, both **Me-Fe** and **F-Fe** initially exhibited CO stretching vibration signals at 2008 and 2048 cm^{-1}, consistent with previously reported observations. The intensity of two absorption peaks gradually decreases under 460 nm LED, accompanied by the emergence of a new absorption signal at 1940 cm^{-1}, indicating the dissociation of a single CO ligand rather than complete release, even under prolonged irradiation. This behavior is markedly different from that observed with P-ligand-coordinated analogs [33], which may be attributed to the

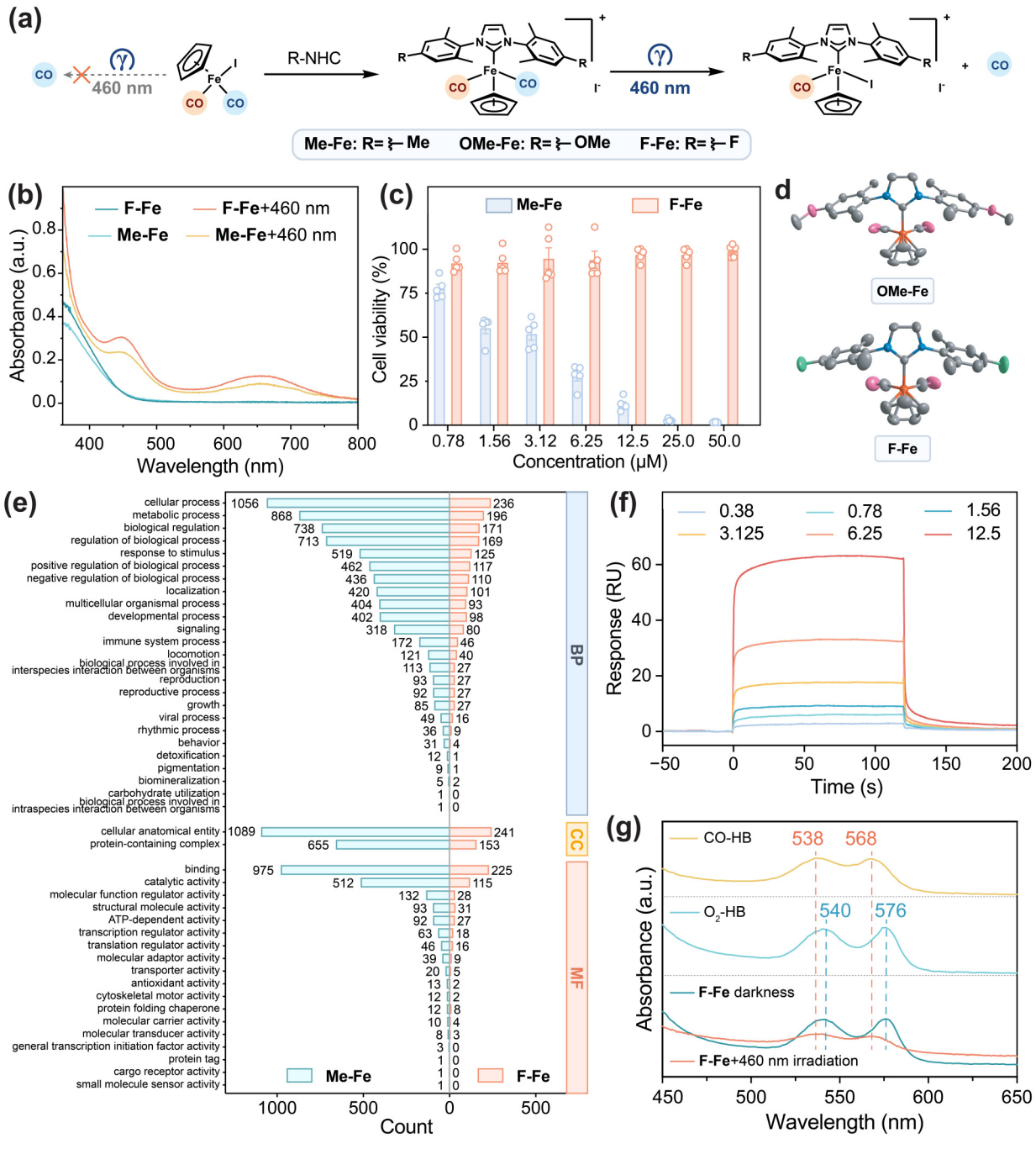

Figure 2 Design and characterization of NHC-Fe CORMs. (a) Molecular design for NHC-Fe CORMs. (b) UV–Vis absorption spectra of **Me-Fe** and **F-Fe** in DCM and the absorption spectra after 460 nm LED irradiation. (c) *In vitro* cytotoxic data in 4T1 cells of **Me-Fe** and **F-Fe** (n = 5). (d) Molecular structure (50% probability of thermal ellipsoids) of **OMe-Fe** (left) and **F-Fe** (right) determined by scXRD with Fe in orange, C in grey, N in blue, O in pink, and F in green. Hydrogen atoms as well as counter ions were omitted. (e) GO level 2 annotation of candidate protein targets for **Me-Fe** (left) and **F-Fe** (right). Bar plots show the numbers of proteins in each GO category (BP, MF, CC), with counts labeled above the bars. (f) SPR analysis showing the affinity of **F-Fe** for the mitochondrial complex IV protein. (g) UV–Vis absorption spectra of Hb coordinated with CO (top), O_2 (middle), and the absorbance change of the solution containing Hb and **F-Fe** after 460 nm LED irradiation in 1 min.

strong σ-donor effect of the NHC ligand and enhances π-back donation from Fe to the remaining CO. Kinetic fitting data for both compounds showed that CO release followed first-order reaction kinetics. The release rate for **F-Fe** (K_{CO} = 0.24 min^{-1}) was slightly higher than that of **Me-Fe** (K_{CO} = 0.13 min^{-1}) (Fig. 3(d)), in line with the trend from DFT calculation (Fig. S24 in the ESM).

Subsequently, the pharmacodynamics of **F-Fe** were validated *in vitro*. To assess the on-target release of CO, we designed a chip with immobilized mitochondrial complex IV and verified it using SPR (Figs. 3(e) and 3(f)). Under dark conditions, the complex IV rapidly and reversibly combined with **F-Fe**, generating strong SPR signals that confirmed its on-target affinity (Fig. 3(f)). Upon light activation, the CO released from **F-Fe** bound to complex IV in an almost non-dissociable condition, resulting in a strong and persistent SPR signal during the dissociation phase, consistent with previous reports on CO-mediated inhibition of cytochrome *c*

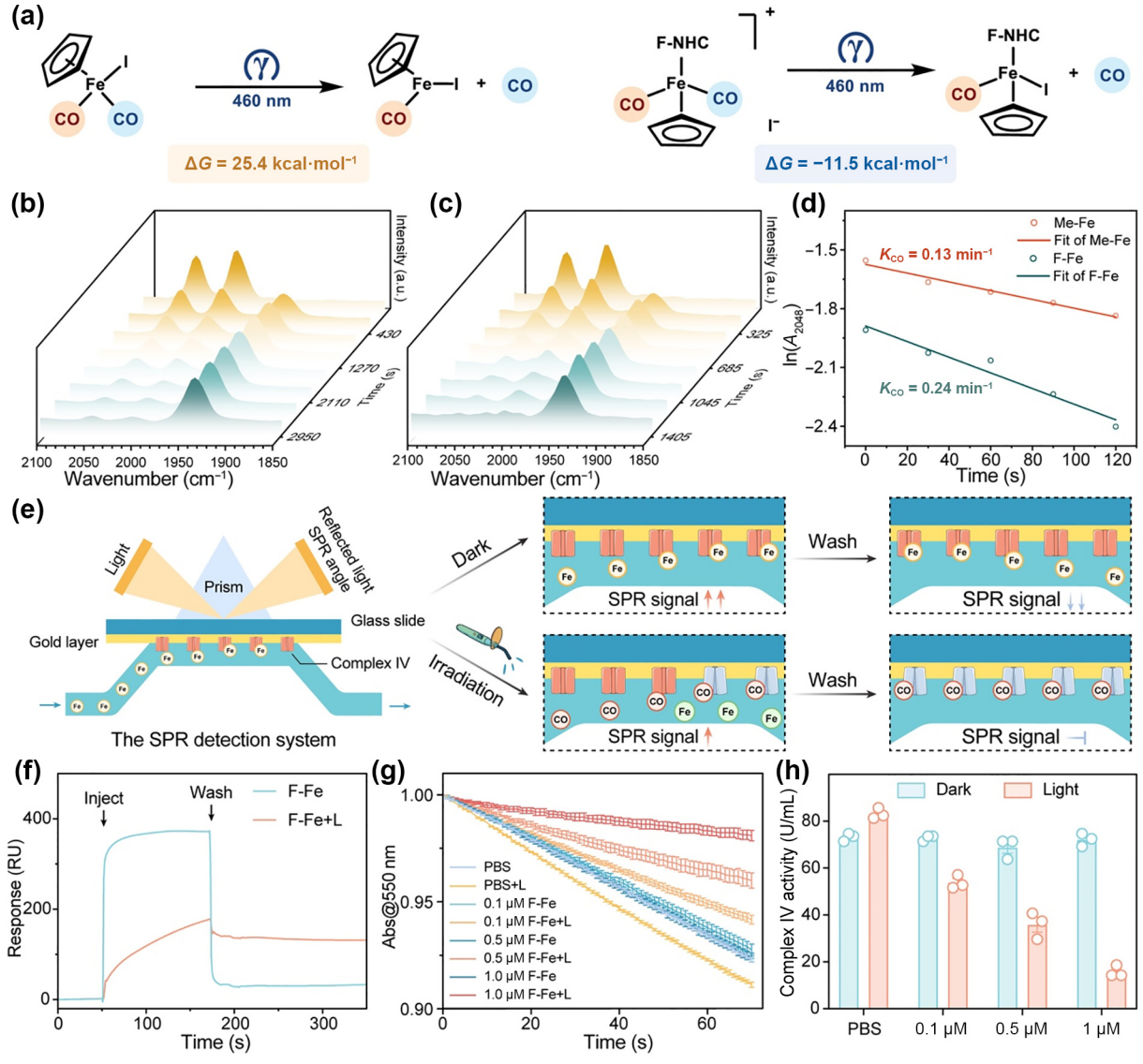

Figure 3 Pharmacological evaluation of NHC-Fe CORMs. (a) The comparison of Δ*G* in the photo-induced CO release process of $CpFe(CO)_2I$ and F-Fe. (b) *In situ* infrared (IR) spectroscope of **Me-Fe** in DCM with 460 nm LED irradiation. (c) *In situ* IR spectroscope of **F-Fe** in dichloromethane (DCM) with 460 nm LED irradiation. (d) Kinetic analysis of **Me-Fe** and **F-Fe** based on *in situ* IR data at 2048 cm^{-1}. (e) Schematic illustration of SPR monitoring of **F-Fe** interactions with complex IV before and after irradiation. (f) SPR analysis showing the combination of **F-Fe** and CO for the mitochondrial complex IV protein. (g) Kinetic curve of mitochondrial complex IV-catalyzed cyt *c* oxidation reaction ($n = 3$). (h) Quantitative analysis of mitochondrial complex IV enzyme activity under different treatments ($n = 3$).

oxidase [5, 7]. UV–Vis spectroscopic monitor of CcO enzymatic activity further demonstrated that, upon administration of **F-Fe**, dental light exposure effectively inhibited CcO function (Figs. 3(g) and 3(h)), suggesting the capability of **F-Fe** to serve as a mitochondrial complex IV-targeting Fe-CORM activatable by clinically approved dental LCU.

3.2 Tumor cell pyroptosis induced by dental light-activated F-Fe

Building on its favorable biocompatibility and on-target activity performance, we investigated the *in vitro* antitumor efficacy of **F-Fe** and explored the mechanisms by which it induces tumor cell death (Fig. 4(a)). LC-MS analysis confirmed the rapid intracellular uptake of **F-Fe** by tumor cells, with quantification showing efficient membrane permeation within minutes (Fig. 4(c), and Fig. S26 in the ESM). Across a range of human and mouse cancer cell lines, including CAL 27 (human OSCC), MCF-7 and HCC1937 (human breast cancer), HCT-15 (human colorectal adenocarcinoma), 4T1 (mouse breast cancer), SCC7 and 4MOSC1 (mouse OSCC), **F-Fe** consistently exhibited low dark toxicity and high phototoxicity under irradiation with dental LCU (Figs. 4(c) and 4(d), and Fig. S27 in the ESM). Under dark conditions, **F-Fe** had minimal effect on the OCR in tumor cells. However, upon light activation, a marked reduction in basal, ATP-linked, and maximal respiration was observed (Fig. 4(e)). This inhibition can be attributed to CO released during phototherapy, which competitively blocks O_2 binding at the reduced heme a_3-Cu_b center of mitochondrial complex IV, thereby disrupting the electron transport chain [7], and potentially triggering mitochondrial stress that leads to cell death [36].

Notably, tumor cells undergoing **F-Fe** mediated phototherapy exhibited a distinctive swollen, balloon-like morphology under optical microscopy, a hallmark of pyroptosis observed consistently

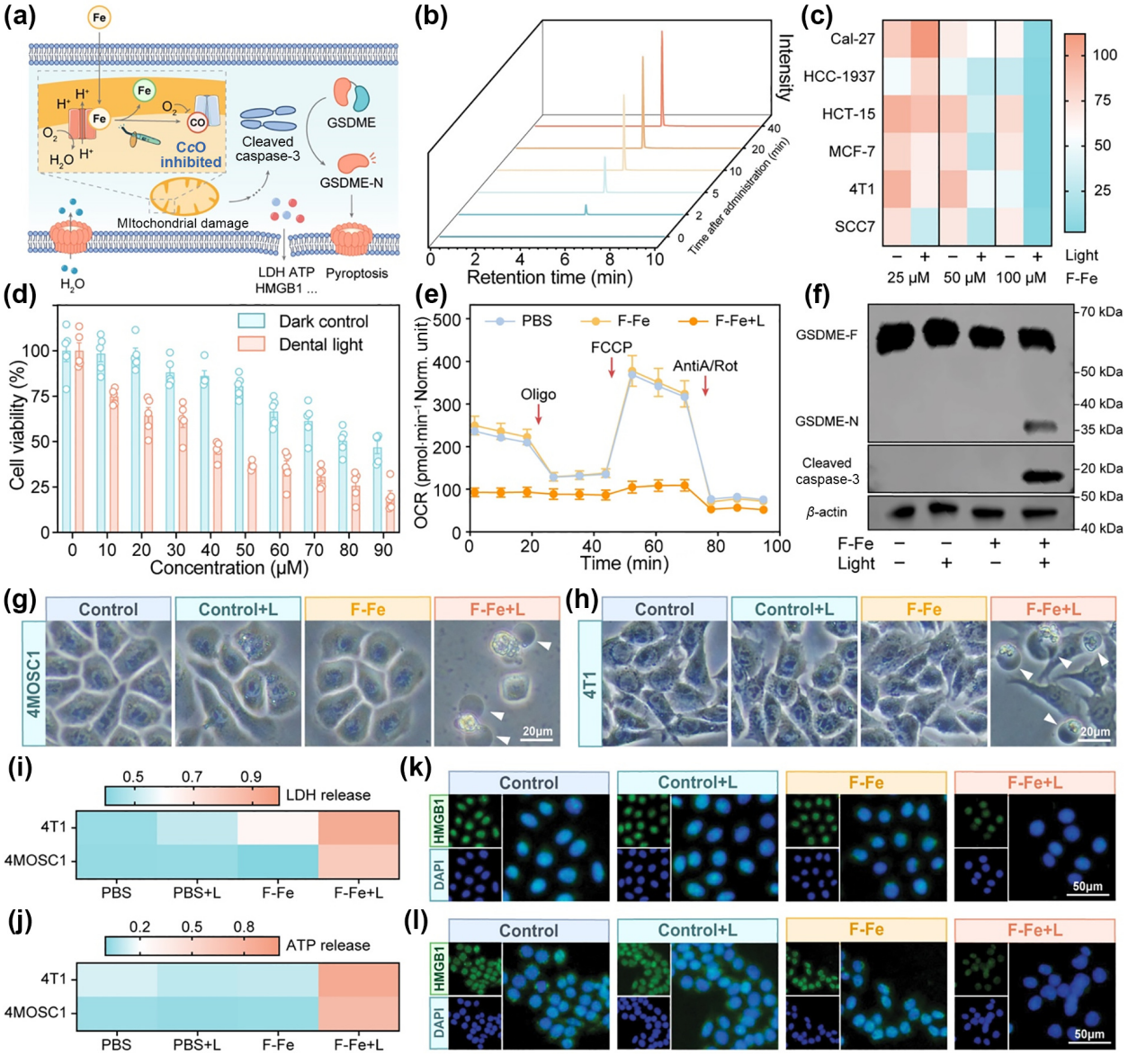

Figure 4 **F-Fe** CORM induces pyroptosis of cancer cells. (a) Schematic illustration of the mechanism by which **F-Fe** induces pyroptosis upon dental LCU irradiation. (b) Chromatograms of LC-MS analysis showing cellular uptake of **F-Fe**. (c) Heat map showing the cytotoxicity of **F-Fe** at varying concentrations in multiple cancer cell under dark or light conditions (n = 5). (d) Phototoxicity and dark toxicity of **F-Fe** in 4MOSC1 oral squamous cell carcinoma (OSCC) cells (n = 5). (e) OCR of cells following different treatments, with responses to oligomycin, FCCP, and antimycin A/rotenone. (f) Cleaved caspase-3 and full length GSDME, and active GSDME-N fragment by western blot analysis. (g) Morphological changes of 4MOSC1 and (h) 4T1 cancer cells after **F-Fe** treatment (scale bars: 20 μm). (i) Quantification of LDH release and (j) ATP secretion following phototherapy (n = 6). (k) Immunofluorescence staining of HMGB1 retention in the nuclei of 4MOSC1 and (l) 4T1 cells (scale bars: 50 μm).

across both 4MOSC1 and 4T1 cell lines (Figs. 4(g) and 4(h)). Pyroptosis is a GSDMs-dependent process initiated by caspase-mediated cleavage of full-length GSDMs, releasing the N-terminal domains (GSDM^{NT}) that oligomerize to form pores in cellular and organelle membranes. This pore formation leads to the membrane blebbing and progressive ballooning, ultimately resulting in osmotic lysis and cell death [37]. Previous studies have demonstrated that CO exerts context-dependent effects by modulating distinct pyroptotic pathways. In the canonical pathway, low doses of CO inhibit the NLRP3/caspase-1/GSDMD axis, thereby conferring cytoprotection against acute lung injury, traumatic brain injury, and ischemia-reperfusion injury [38]. Conversely, at the high doses typically employed for anti-tumor applications, CO triggers the non-canonical caspase-3 pathway, driving GSDME-mediated pyroptosis [39]. In this study, western blot revealed that mitochondrial stress induced the activation of executioner caspase-3 (Fig. 4(f)). Consistent with previous reports [40], activated caspase-3 cleaved GSDME to release the pore-forming GSDME^{NT} (Fig. 4(f)), thereby converting the cell death modality from apoptosis to pyroptosis.

Excitingly, beyond directly inducing tumor cell death, pyroptosis that characterized by plasma membrane rupture represents a proinflammatory form of programmed cell death with the potential to remodel the TME and enhance antitumor immunity [37, 41]. *In vitro*, **F-Fe**-mediated phototherapy significantly increased the release of LDH (Fig. 4(i)), a marker of plasma membrane rupture, along with elevated ATP concentrations in the supernatant

(Fig. 4(j)), a potent chemokine for dendritic cells (DCs) recruitment [42, 43]. Concurrently, immunofluorescence staining revealed the reduction in nuclear HMGB1, indicated its release into the extracellular environment (Fig. 4(l)), where it acts as a chemoattractant and proinflammatory signal [41]. These danger-associated molecular patterns (DAMPs) suggest that **F-Fe** phototherapy not only induces mitochondrial stress-mediated cytotoxicity but also holds promise for reprogramming the TME, thereby eliciting robust and durable antitumor immune responses.

3.3 GLEAM for bio-adhesive and light-guided delivery in Fe-based phototherapy

Firm adhesion to rough tissue surfaces, minimally invasive and precise drug delivery, and effective light transmission through biological barriers are essential for enabling efficient *in vivo* phototherapy with **F-Fe**. Inspired by *O. vulgaris*, a remarkable marine predator, we engineered a GLEAM system that mimics the organism's efficient penetrating beak and adhesive suckers [32, 44], and integrates a photonic delivery architecture to support deep-tissue CORM therapy (Fig. 5(a) and Fig. S29 in the ESM).

To further facilitate the deep delivery of photonic energy, we engineered an integrated light-guiding architecture within the microneedle system. Previous research indicates that embedding light-guiding microstructures in microneedles effectively increases the tissue penetration depth of high-energy photons [31, 45]. Based on the principle of total internal reflection, these structures can efficiently deliver blue and even UV photons deep into tissues [31], which is especially crucial when crossing skin and mucosal barriers. Therefore, a cone-shaped light-guiding array with flattened tips was positioned on the base layer of GLEAM. The positive model of the base was fabricated by 3D printing using HTL resin (Fig. S30 in the ESM). Subsequently, a negative mold was created by embedding the resin structure in PDMS. PVA hydrogels, selected for their excellent biocompatibility and visible-light transmittance [46], were cast into the PDMS mold to form the translucent base with light-guiding cone (Fig. S31 in the ESM). The successful fabrication of the light-guiding layer was confirmed by optical imaging and transmission electron microscopy (Figs. 5(b) and 5(c)).

Unlike other cephalopods, the suckers of *O. vulgaris* feature a distinct internal protuberance at the orifice [32]. The specialized anatomical structure has led some researchers to hypothesize that,

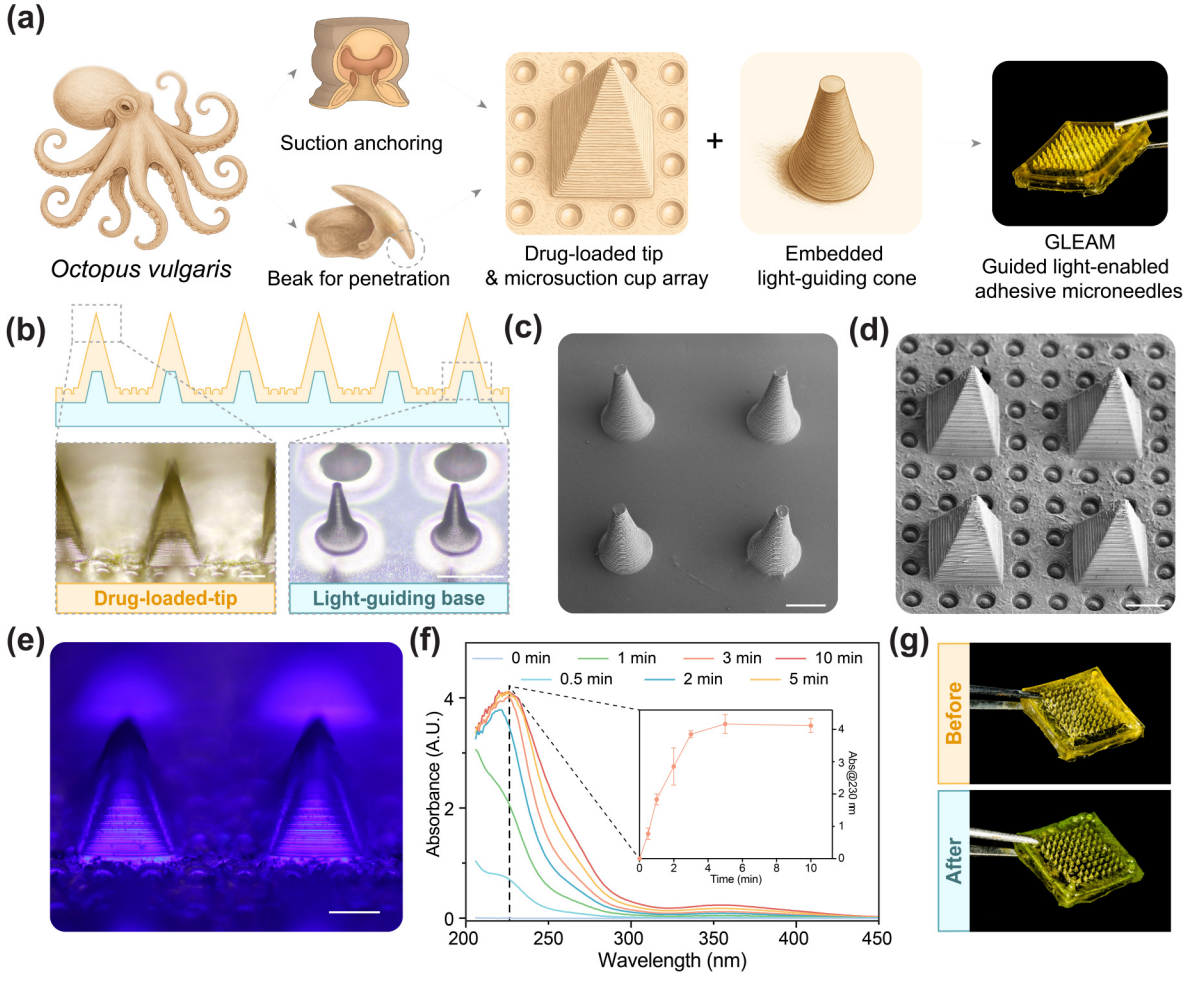

Figure 5 Design and characterization of Fe-GLEAM. (a) Schematic illustration of the *O. vulgaris*-inspired GLEAM, featuring drug loaded dissolvable tips for **F-Fe** delivery, peripheral micro-suction cups, and embedded light-guiding cones. (b) Bright-field image of the GLEAM surface and base structure (scale bars: 200 μm). (c) SEM images showing the embedded light-guiding cone, and (d) the drug-loaded tips surrounded by micro-suction structures (scale bars: 200 μm). (e) Fluorescence imaging of the microneedles showing the rhodamine B labeled light-guiding cone (red fluorescence) embedded within the GLEAM (scale bar: 200 μm). (f) *In vitro* **F-Fe** release from the Fe-GLEAM as measured by UV–Vis spectroscopy (n = 3). (g) Light-triggered color change of the GLEAM under irradiation by dental LCU, enabling visible feedback during treatment.

beyond the widely acknowledged active muscular hydrostatic pressure actuations utilized in bioinspired robotics [47], it may also contribute to adhesion via a passive attachment mechanism [32, 48], offering a promising strategy for microneedle adhesion design (Fig. 5(a)). Specifically, the dome-shaped bioinspired structure can generate liquid-assisted suction when miniaturized to the micrometer scale, enabling robust adhesion on both dry and moist rough tissue surfaces [49]. These adhesive units were densely arrayed around each microneedle tip on the patch backing (Figs. 5(b) and 5(d)), allowing each GLEAM device to carry a high density of suction interfaces that collectively ensure firm and reliable attachment during phototherapy (Fig. S32 in the ESM).

To mimic the tapered geometry of the *O. vulgaris* beak and facilitate penetration through keratinized epithelium, the GLEAM tip was designed with a pyramidal architecture (Fig. 5(a) and Fig. S29 in the ESM). Using the same fabrication approach, we 3D-printed a mold for the GLEAM insertion tips and replicated it with PDMS (Figs. S29 and S30 in the ESM). **F-Fe** was mixed into hyaluronic acid (HA) and cast onto the light-guiding PVA base layer, forming the drug-loaded, dissolvable insertion module of the GLEAM system (Figs. 5(b) and 5(d), and Fig. S29 in the ESM). SEM revealed that GLEAM featured well-defined, uniformly distributed pyramidal tips surrounded by densely arranged bioinspired adhesive structures (Fig. 5(d)). The optical microscope further confirmed the embedding of the light-guiding cone beneath the insertion tip, and the distinct orange-yellow coloration of the microneedle surface indicated successful loading of **F-Fe** (Figs. 5(a) and 5(b)). By labeling the PVA-based light-guiding layer with rhodamine B, fluorescence microscopy showed bright red emission from the embedded cone, while the overlying **F-Fe** loaded HA tips appeared dark due to blue-light absorption (Fig. 5(e)). *In vitro* dissolving experimental result demonstrated that the insertion tips rapidly dissolved within minutes, enabling efficient release of the encapsulated **F-Fe** from the outer HA layer (Fig. 5(f) and Fig. S34 in the ESM). Consistently, photography and H&E staining of skin and oral cancer tissue confirmed the ability of GLEAM to penetrate tissue and deliver **F-Fe** effectively (Fig. S33 in the ESM). Notably, the photolysis of orange-yellow **F-Fe** under dental LCU irradiation yielded the green-colored product, allowing real-time monitoring of microneedle treatment (Fig. 5(g), and Figs. S20 and S21 in the ESM). Given that green is complementary to the reddish appearance of most mucosal and biological tissues, this pronounced color shift provides clear visualization of treatment progression. This optical feedback may facilitate intra-procedural guidance in subsequent *in vivo* treatment.

3.4 *In vivo* tumor suppression and immune-microenvironment reprogramming by Fe-GLEAM

The murine 4MOSC1 cell line [50, 51] was employed to establish an orthotopic OSCC model, representative of the most common superficial malignancy in the oropharyngeal region [52], to evaluate the feasibility of Fe-GLEAM for *in vivo* treatment (Fig. 6(a)). Additionally, a subcutaneous 4T1 breast cancer model implanted in the dorsal region of mice was used to further corroborate the generalizability of this approach (Fig. S35 in the ESM). Fe-GLEAM phototherapy significantly suppressed OSCC growth in mice relative to control and sham-treated groups (Figs. 6(b) and 6(c)), leading to recovery of tumor-induced body weight loss (Fig. 6(d)). In the subcutaneous 4T1 breast cancer model, Fe-GLEAM similarly demonstrated potent antitumor activity, with stable body weights throughout the treatment period supporting its safety (Fig. S35 in the ESM).

Post-treatment histopathological examination of major organs revealed no evident tissue damage (Fig. S36 in the ESM), and hematological and serum biochemical analyses showed no significant abnormalities (Tables S2 and S3 in the ESM), further confirming the safety of Fe-GLEAM phototherapy.

Previous studies show that pyroptosis remodels the TME by releasing DAMPs and cytokines that enhance antitumor immunity [41]. Consistent with these findings, our *in vitro* experiments revealed robust production of these immunostimulatory DAMPs following treatment (Fig. 4).

Moreover, CO generated by photochemical activation has been shown to modulate multiple immunological processes [5–8]. Based on these observations, we further investigated the changes within the tumor immune landscape induced by Fe-GLEAM phototherapy. In the TDLNs, Fe-GLEAM phototherapy promoted the maturation of DCs ($CD80^+CD86^+$) (Fig. 6(i), and Figs. S37 and S38 in the ESM), thereby enhancing their antigen-presenting capacity and facilitating the priming and expansion of tumor-specific T cells, as evidenced by the increased proportions of $CD3^+CD4^+$ and $CD3^+CD8^+$ T cells (Figs. 6(j)–6(l), and Figs. S39 and S40 in the ESM).

Within the tumor, we observed substantial infiltration of cytotoxic $CD8^+$ T cells expressing elevated levels of GZMB (Fig. 6(e)), indicating their cytotoxic activity. Concurrently, the infiltration of immunosuppressive M2-like TAMs ($F4/80^+CD206^+$) was significantly reduced, while pro-inflammatory M1-like macrophages ($F4/80^+MHCII^+$) were increased, highlighting a reprogrammed milieu favoring antitumor immunity (Figs. 6(f)–6(h), and Figs. S41 and S42 in the ESM). Notably, Fe-GLEAM phototherapy not only promoted the differentiation of T cells toward effector phenotypes but also facilitated the generation of memory subsets. In the TDLNs, the proportions of both $CD4^+$ and $CD8^+$ central memory T cells (T_{CM}, $CD44^+CD62L^+$) were significantly increased (Figs. 6(m) and 6(n), and Fig. S40 in the ESM), suggesting the establishment of durable antitumor immune memory. Collectively, these findings demonstrate that GLEAM therapy not only mediates direct tumor cell eradication via pyroptosis but also remodels the TME to support sustained antitumor immunity.

3.5 Fe-GLEAM enhances immune checkpoint blockade for synergistic tumor therapy

Given that Fe-GLEAM induces pyroptosis-mediated T cell infiltration and fosters a relatively hot TME, it holds promise for enhancing responsiveness to ICB and enabling combination therapy [53]. In the orthotopic OSCC model (Fig. 7(a)), tumor growth curves revealed that combination therapy nearly eradicated tongue tumors (Fig. 7(b)), with all mice in the Fe-GLEAM combined with αPD-1 treatment group ($n = 5$) surviving until the end of the study (Fig. 7(c)). Given that metastasis is a leading cause of cancer-related mortality [54], we further established a dual-flank breast cancer model to evaluate the systemic efficacy of the combination treatment. Specifically, 4T1 cells were first inoculated into the right flank to form a primary tumor, followed 2 days later by contralateral implantation of tumor cells to mimic a distal metastatic lesion. Fe-GLEAM phototherapy was applied locally to the primary tumor, while systemic aPD-1 blockade was administered (Fig. 7(d)). Tumor growth curves demonstrated that

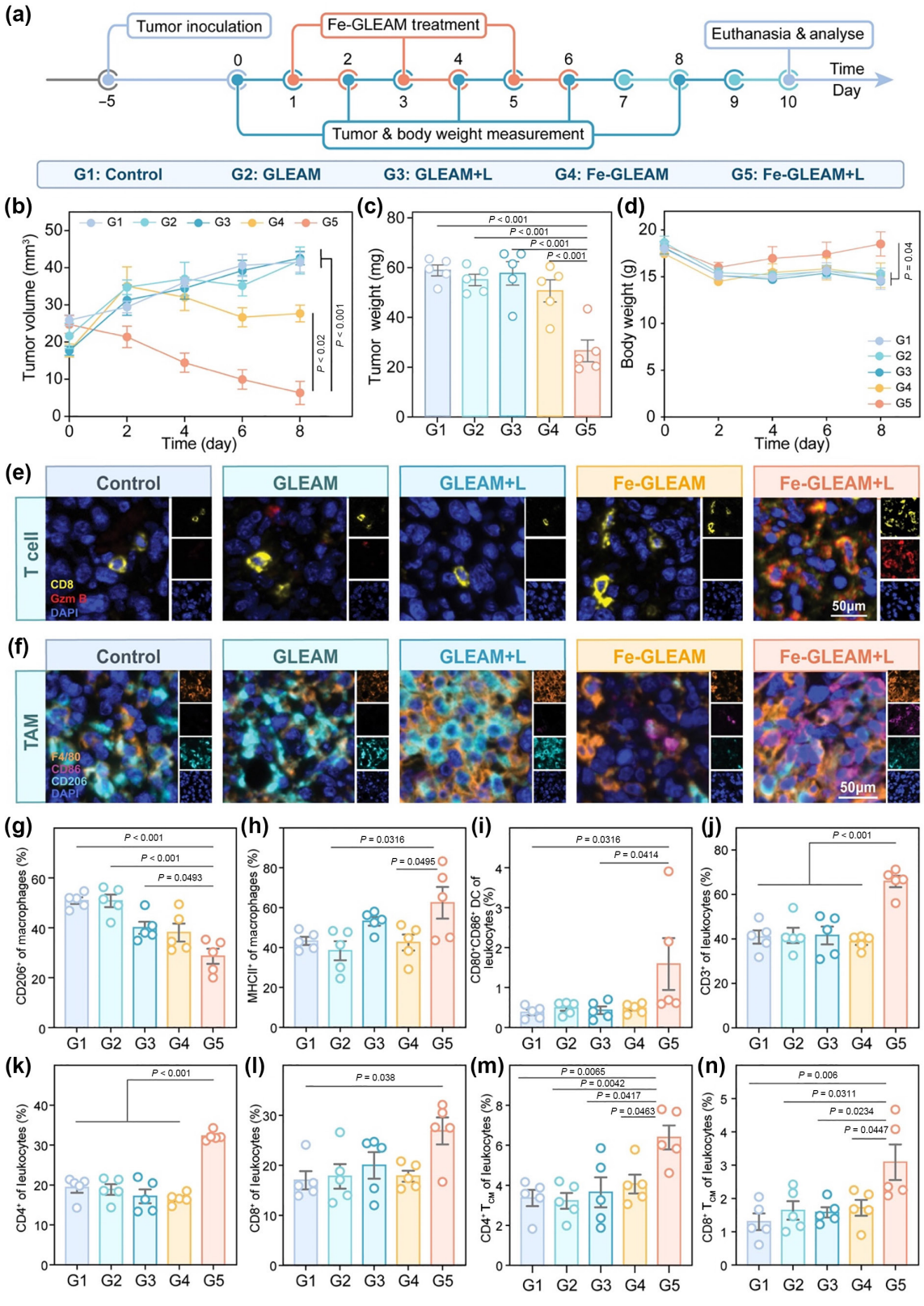

Figure 6 *In vivo* antitumor efficacy and TME remodeling by Fe-GLEAM treatment. (a) Schematic illustration of the treatment schedule and experimental grouping *in vivo*. (b) Tumor volume curves following different treatments. (c) Tumor weight at the end of treatment. (d) Body weight changes of oral cancer-bearing mice. (e) Multiplex immunohistochemical (mIHC) analysis of T cells and (f) tumor-associated macrophage (TAM). (g) Quantification of M2-like (F4/80⁺CD206⁺) and (h) M1-like (F4/80⁺MHCII⁺) macrophages in tumor. (i) Quantification of mature DCs (CD80⁺CD86⁺) in TDLNs by flow cytometry. Flow cytometric analysis of (j) CD3⁺, (k) CD4⁺, and (l) CD8⁺ T cell populations among CD45⁺ lymphocytes in the TDLNs. Quantification of central memory T cells (CD44⁺CD62L⁺), including (m) CD4⁺ and (n) CD8⁺ subsets, in TDLNs. G1: Control group; G2: Placebo GLEAM without light irradiation; G3: Placebo GLEAM with light irradiation; G4: **F-Fe**-loaded GLEAM (Fe-GLEAM) without light irradiation; G5: Fe-GLEAM with light irradiation ($n = 5$).

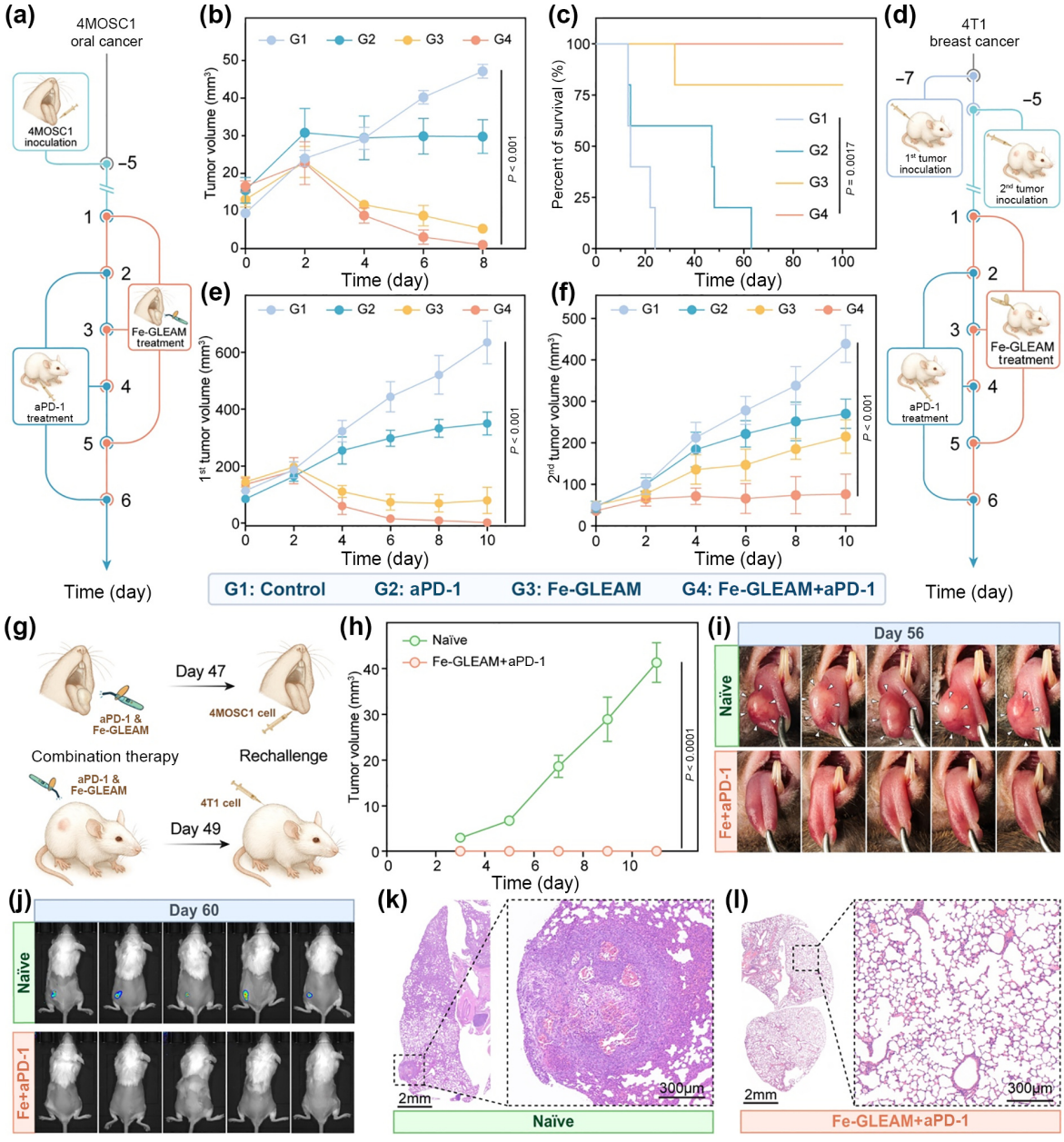

Figure 7 Fe-GLEAM potentiates aPD-1 immunotherapy and elicits durable immune memory. (a) Schematic of the treatment schedule for the orthotopic OSCC model. (b) Tumor growth curves of OSCC under different treatments. (c) Kaplan-Meier survival curves of OSCC-bearing mice. (d) Schematic of the treatment schedule for the breast cancer model. (e) Primary tumor and (f) secondary tumor growth curves in breast cancer mice following different treatments. (g) Experimental design for tumor rechallenge in OSCC and breast cancer mice. (h) Tumor volume curves after OSCC rechallenge in naïve and combination-treated mice (n = 5). (i) Photograph of the tongue after OSCC-rechallenge. (j) *In vivo* bioluminescence imaging of breast tumor burden after 4T1 rechallenge in naïve and combination-treated mice. Representative hematoxylin and eosin (H&E) staining of lung sections showing metastatic lesions after breast cancer cell rechallenge in (k) naïve mice and (l) combination-treated mice (n = 5). G1: Control group; G2: aPD-1 monotherapy group; G3: Fe-GLEAM therapy; G4: Combination therapy with Fe-GLEAM and aPD-1.

while Fe-GLEAM treatment targeted the primary tumor and induced significant regression, the combination with aPD-1 blockade further suppressed the growth of distal tumor lesions, highlighting a potent systemic antitumor response (Figs. 7(e) and 7(f)).

Tumor recurrence represents another major challenge that compromises the long-term survival and quality of life in cancer patients [55]. Building on the potent antitumor efficacy of Fe-GLEAM and its capacity to induce immunological memory, we reasoned that combining this strategy with ICB could effectively suppress both tumor relapse and metastasis. To validate this hypothesis, we established orthotopic OSCC and subcutaneous breast cancer rechallenge models (Fig. 7(g)). Following 7 weeks of tumor-free survival after the combination therapy, rechallenge with the same tumor cells did not result in tumor regrowth in either the OSCC or breast cancer mice (Figs. 7(h)–7(j), and Fig. S43 in the ESM). By contrast, naïve control mice inoculated with the identical cell lines developed progressive tumors, highlighting the induction of robust and durable antitumor immune memory. Consistent with these findings, the combination treatment effectively suppressed distant tumor metastasis (Figs. 7(k) and 7(l)), and all mice subjected to rechallenge exhibited sustained tumor-free survival (Figs. S44

and S45 in the ESM), demonstrating that this strategy elicited a remarkable and durable therapeutic response.

4 Conclusions

Iron, the most abundant transition metal in Earth's crust, has shaped biological evolution as a primordial redox catalyst [11]. Its central role in redox biology, together with its wide availability and geological abundance, positions it as a promising candidate for addressing the escalating demand for cancer therapeutics. Here, we demonstrate that structure-activity guided design of Fe-NHC complexes, combined with biomimetic delivery strategies, enables the development of iron-based anticancer therapeutics with on-target activity and clinical promise.

With the advent of cancer immunotherapy in clinical practice, the immunosuppressive TME remains a major barrier limiting its benefits for many patients [4]. Using the GLEAM system to deliver the complex IV-targeted CORM **F-Fe**, and guiding photons from clinically approved dental LCUs to deeper tissue, we achieved on-target CO release that triggered pyroptosis and effectively remodeled the TME. The strategy markedly enhanced aPD-1 therapy, significantly suppressed metastasis and recurrence, and promoted durable immune memory that extended tumor-free survival in mice. Against the backdrop of a rising global cancer incidence [52], these findings suggest that iron, owing to its abundance and bioactivity, may provide a viable basis for precise and sustainable antitumor strategies, particularly considering global inequalities in cancer burden [2] and increasing concerns about financial toxicity [56] of cancer therapies.

Electronic Supplementary Material: Supplementary material (detailed experimental procedures, synthetic protocols and characterization data, supporting CO-release measurements, DFT calculation details, GLEAM fabrication and characterization procedures, additional *in vitro* and *in vivo* biological evaluations, biosafety analyses, and flow cytometry gating strategies) is available in the online version of this article at https://doi.org/10.26599/NR.2026.94908830.

Data availability

All data needed to support the conclusions in the paper are presented in the manuscript and the Electronic Supplementary Material. Additional data related to this paper may be requested from the corresponding author upon request.

Acknowledgements

This work was supported by the National Key R&D Program of China (Nos. 2021YFA1500100 and 2022YFA1505100), the National Natural Science Foundation of China (No. 22031008, A. W. L.; No. 82273202, Z.-J. S.; No. 22522112, H. Y.; No. 225B2118, H. Z. D.), Hubei Technological Innovation Program Funding (No. 2025BAB025), and the Fundamental Research Funds for the Central Universities (Nos. 2042022dx0003 and 2042024kf0021, Z.-J. S.). We thank Dr. Wen-Ting Fan from the Core Facility of Wuhan University for her assistance with SEM measurements. The authors would like to thank the Core Facility of Wuhan University for LC-MS analysis. The authors also thank Dr. Min Pan, Medical Research Institute of Wuhan University, for the technical assistance. We would like to thank the Medical Research for Structural Biology of Basic Medical Sciences, Wuhan University, for the technical help of flow cytometry. We thank Shanghai Bioprofile Technology Co., Ltd. for their support with limited proteolysis-coupled mass spectrometry technology.

Declaration of competing interest

All the contributing authors report no conflict of interests in this work.

Author contribution statement

W.-Y. W., H. Z. D., and H. Y. contributed to the conception of the study. W.-Y. W. and H. Z. D. designed the research, generated the figures, and wrote the manuscript. E.-L. Y. and Q. W. assisted with cell culture and animal studies, and N. C. contributed to the chemical synthesis. Z. Q. Z. analyzed the scXRD data. X. Q. H. conducted the quantum chemical calculations. H. Y., A. W. L., and Z.-J. S. directed and coordinated the study, and provided guidance on experimental design and data interpretation. All authors discussed the results and reviewed the manuscript.

Informed consent

Not applicable.

Ethics statement

Animal experiments were reviewed and approved by the Ethics Committee for Experimental Animals of the School and Hospital of Stomatology, Wuhan University (approval number: S07923030F). All procedures were conducted in accordance with the Regulations for the Administration of Affairs Concerning Experimental Animals, issued by the State Council of the People's Republic of China.

Use of AI statement

None.

References

[1] Soerjomataram, I.; Bray, F. Planning for tomorrow: Global cancer incidence and the role of prevention 2020-2070. *Nat. Rev. Clin. Oncol.* **2021**, *18*, 663–672.

[2] Sung, H.; Ferlay, J.; Siegel, R. L.; Laversanne, M.; Soerjomataram, I.; Jemal, A.; Bray, F. Global cancer statistics 2020: GLOBOCAN estimates of incidence and mortality worldwide for 36 cancers in 185 countries. *CA Cancer J. Clin.* **2021**, *71*, 209–249.

[3] Korman, A. J.; Garrett-Thomson, S. C.; Lonberg, N. The foundations of immune checkpoint blockade and the ipilimumab approval decennial. *Nat. Rev. Drug Discov.* **2022**, *21*, 509–528.

[4] Bell, H. N.; Zou, W. P. Beyond the barrier: Unraveling the mechanisms of immunotherapy resistance. *Annu. Rev. Immunol.* **2024**, *42*, 521–550.

[5] Yuan, Z. N.; De La Cruz, L. K.; Yang, X. X.; Wang, B. H. Carbon monoxide signaling: Examining its engagement with various molecular targets in the context of binding affinity, concentration, and biologic response. *Pharmacol. Rev.* **2022**, *74*, 825–875.

[6] Xiao, X.; Liang, S.; Zhao, Y. J.; Pang, M. L.; Ma, P.; Cheng, Z. Y.; Lin, J. Multifunctional carbon monoxide nanogenerator as immunogenic cell death drugs with enhanced antitumor immunity and antimetastatic effect. *Biomaterials* **2021**, *277*, 121120.

[7] Chakraborty, P.; Parikh, R. Y.; Choi, S.; Tran, D.; Gooz, M.; Hedley,

Z. T.; Kim, D. S.; Pytel, D.; Kang, I.; Nadig, S. N. et al. Carbon monoxide activates PERK-regulated autophagy to induce immunometabolic reprogramming and boost antitumor T-cell function. *Cancer Res.* **2022**, *82*, 1969–1990.

[8] Oza, P. P.; Kashfi, K. The triple crown: NO, CO, and H_2S in cancer cell biology. *Pharmacol. Ther.* **2023**, *249*, 108502.

[9] Peña, Q.; Wang, A.; Zaremba, O.; Shi, Y.; Scheeren, H. W.; Metselaar, J. M.; Kiessling, F.; Pallares, R. M.; Wuttke, S.; Lammers, T. Metallodrugs in cancer nanomedicine. *Chem. Soc. Rev.* **2022**, *51*, 2544–2582.

[10] Wang, W. Y.; Mo, W. T.; Hang, Z. S.; Huang, Y. Y.; Yi, H.; Sun, Z. J.; Lei, A. W. Cuproptosis: Harnessing transition metal for cancer therapy. *ACS Nano* **2023**, *17*, 19581–19599.

[11] Johnson, J. E.; Present, T. M.; Valentine, J. S. Iron: Life's primeval transition metal. *Proc. Natl. Acad. Sci. USA* **2024**, *121*, e2318692121.

[12] Haynes, W. M.; Thomas, D. R. L.; Bruno, J. *CRC Handbook of Chemistry and Physics, 2016-2017*; CRC Press: Boca Raton, 2016.

[13] Jiang, X. J.; Xiao, Z. Y.; Zhong, W.; Liu, X. M. Brief survey of diiron and monoiron carbonyl complexes and their potentials as CO-releasing molecules (CORMs). *Coord. Chem. Rev.* **2021**, *429*, 213634.

[14] Riener, K.; Haslinger, S.; Raba, A.; Högerl, M. P.; Cokoja, M.; Herrmann, W. A.; Kühn, F. E. Chemistry of iron *N*-heterocyclic carbene complexes: Syntheses, structures, reactivities, and catalytic applications. *Chem. Rev.* **2014**, *114*, 5215–5272.

[15] Benito-Garagorri, D.; Alves, L. G.; Veiros, L. F.; Standfest-Hauser, C. M.; Tanaka, S.; Mereiter, K.; Kirchner, K. Kinetically controlled formation of octahedral *trans*-dicarbonyl iron(II) PNP pincer complexes: The decisive role of spin-state changes. *Organometallics* **2010**, *29*, 4932–4942.

[16] Benito-Garagorri, D.; Puchberger, M.; Mereiter, K.; Kirchner, K. Stereospecific and reversible CO binding at iron pincer complexes. *Angew. Chem., Int. Ed.* **2008**, *47*, 9142–9145.

[17] Basu, U.; Roy, M.; Chakravarty, A. R. Recent advances in the chemistry of iron-based chemotherapeutic agents. *Coord. Chem. Rev.* **2020**, *417*, 213339.

[18] Paulus, B. C.; Nielsen, K. C.; Tichnell, C. R.; Carey, M. C.; McCusker, J. K. A modular approach to light capture and synthetic tuning of the excited-state properties of Fe(II)-based chromophores. *J. Am. Chem. Soc.* **2021**, *143*, 8086–8098.

[19] Liu, Y. Z.; Persson, P.; Sundström, V.; Wärnmark, K. Fe *N*-heterocyclic carbene complexes as promising photosensitizers. *Acc. Chem. Res.* **2016**, *49*, 1477–1485.

[20] Hopkinson, M. N.; Richter, C.; Schedler, M.; Glorius, F. An overview of N-heterocyclic carbenes. *Nature* **2014**, *510*, 485–496.

[21] Hickey, J. L.; Ruhayel, R. A.; Barnard, P. J.; Baker, M. V.; Berners-Price, S. J.; Filipovska, A. Mitochondria-targeted chemotherapeutics: The rational design of gold(I) *N*-heterocyclic carbene complexes that are selectively toxic to cancer cells and target protein selenols in preference to thiols. *J. Am. Chem. Soc.* **2008**, *130*, 12570–12571.

[22] Patil, S. A.; Patil, S. A.; Patil, R.; Keri, R. S.; Budagumpi, S.; Balakrishna, G. R.; Tacke, M. *N*-heterocyclic carbene-metal complexes as bio-organometallic antimicrobial and anticancer drugs. *Future Med. Chem.* **2015**, *7*, 1305–1333.

[23] Teyssot, M. L.; Jarrousse, A. S.; Manin, M.; Chevry, A.; Roche, S.; Norre, F.; Beaudoin, C.; Morel, L.; Boyer, D.; Mahiou, R. et al. Metal-NHC complexes: A survey of anti-cancer properties. *Dalton Trans.* **2009**, 6894–6902.

[24] Johnson, C.; Albrecht, M. Piano-stool N-heterocyclic carbene iron complexes: Synthesis, reactivity and catalytic applications. *Coord. Chem. Rev.* **2017**, *352*, 1–14.

[25] Jandt, K. D.; Mills, R. W. A brief history of LED photopolymerization. *Dent. Mater.* **2013**, *29*, 605–617.

[26] Li, D. D.; Hu, D. D.; Xu, H. X.; Patra, H. K.; Liu, X. R.; Zhou, Z. X.; Tang, J. B.; Slater, N.; Shen, Y. Q. Progress and perspective of microneedle system for anti-cancer drug delivery. *Biomaterials* **2021**, *264*, 120410.

[27] Khan, S.; Hasan, A.; Attar, F.; Babadaei, M. M. N.; Zeinabad, H. A.; Salehi, M.; Alizadeh, M.; Hassan, M.; Derakhshankhah, H.; Hamblin, M. R. et al. Diagnostic and drug release systems based on microneedle arrays in breast cancer therapy. *J. Control. Release* **2021**, *338*, 341–357.

[28] Edwards, C.; Shah, S. A.; Gebhardt, T.; Jewell, C. M. Exploiting unique features of microneedles to modulate immunity. *Adv. Mater.* **2023**, *35*, 2302410.

[29] Zhu, Z.; Wang, J.; Pei, X. B.; Chen, J. Y.; Wei, X. W.; Liu, Y. H.; Xia, P. C.; Wan, Q. B.; Gu, Z.; He, Y. Blue-ringed octopus-inspired microneedle patch for robust tissue surface adhesion and active injection drug delivery. *Sci. Adv.* **2023**, *9*, eadh2213.

[30] Yang, C. W.; Sheng, T.; Hou, W. H.; Zhang, J.; Cheng, L.; Wang, H.; Liu, W.; Wang, S. Q.; Yu, X. M.; Zhang, Y. Q. et al. Glucose-responsive microneedle patch for closed-loop dual-hormone delivery in mice and pigs. *Sci. Adv.* **2022**, *8*, eadd3197.

[31] Lee, Y.; Kang, T.; Cho, H. R.; Lee, G. J.; Park, O. K.; Kim, S.; Lee, B.; Kim, H. M.; Cha, G. D.; Shin, Y. et al. Localized delivery of theranostic nanoparticles and high-energy photons using microneedles-on-bioelectronics. *Adv. Mater* **2021**, *33*, 2100425.

[32] Tramacere, F.; Kovalev, A.; Kleinteich, T.; Gorb, S. N.; Mazzolai, B. Structure and mechanical properties of *Octopus vulgaris* suckers. *J. R. Soc. Interface* **2014**, *11*, 20130816.

[33] Catheline, D.; Astruc, D. Bis- and tris-acetonitrile complexes of iron(II). *J. Organomet. Chem.* **1983**, *248*, c9–c12.

[34] Schopper, S.; Kahraman, A.; Leuenberger, P.; Feng, Y. H.; Piazza, I.; Müller, O.; Boersema, P. J.; Picotti, P. Measuring protein structural changes on a proteome-wide scale using limited proteolysis-coupled mass spectrometry. *Nat. Protoc.* **2017**, *12*, 2391–2410.

[35] Dawson, J. H.; Sono, M. Cytochrome p-450 and chloroperoxidase: Thiolate-ligated heme enzymes. spectroscopic determination of their active-site structures and mechanistic implications of thiolate ligation. *Chem. Rev.* **1987**, *87*, 1255–1276.

[36] Chipuk, J. E.; Mohammed, J. N.; Gelles, J. D.; Chen, Y. Y. Mechanistic connections between mitochondrial biology and regulated cell death. *Dev. Cell* **2021**, *56*, 1221–1233.

[37] Broz, P.; Pelegrín, P.; Shao, F. The gasdermins, a protein family executing cell death and inflammation. *Nat. Rev. Immunol.* **2020**, *20*, 143–157.

[38] Li, H. J.; Hao, M. Y.; Han, H. S.; Chu, T.; Wang, Y. W.; Si, W. R.; Jiang, Q. Y.; Wu, D. D. Role of gasotransmitters in pyroptosis. *Int. J. Biol. Macromol.* **2025**, *322*, 146142.

[39] Zhong, H. H.; Chen, G. J.; Li, T.; Huang, J. S.; Lin, M. Z.; Li, B.; Xiao, Z. C.; Shuai, X. T. Nanodrug augmenting antitumor immunity for enhanced TNBC therapy via pyroptosis and cGAS-STING activation. *Nano Lett.* **2023**, *23*, 5083–5091.

[40] Wang, Y. P.; Gao, W. Q.; Shi, X. Y.; Ding, J. J.; Liu, W.; He, H. B.; Wang, K.; Shao, F. Chemotherapy drugs induce pyroptosis through caspase-3 cleavage of a gasdermin. *Nature* **2017**, *547*, 99–103.

[41] Wang, W. Y.; Zhang, L.; Sun, Z. J. Eliciting pyroptosis to fuel cancer immunotherapy: Mechanisms and strategies. *Cancer Biol. Med.* **2022**, *19*, 948–964.

[42] Sáez, P. J.; Vargas, P.; Shoji, K. F.; Harcha, P. A.; Lennon-Duménil, A. M.; Sáez, J. C. ATP promotes the fast migration of dendritic cells through the activity of pannexin 1 channels and $P2X_7$ receptors. *Sci. Signal.* **2017**, *10*, eaah7107.

[43] La Sala, A.; Sebastiani, S.; Ferrari, D.; Di Virgilio, F.; Idzko, M.; Norgauer, J.; Girolomoni, G. Dendritic cells exposed to extracellular adenosine triphosphate acquire the migratory properties of mature cells and show a reduced capacity to attract type 1 T lymphocytes. *Blood* **2002**, *99*, 1715–1722.

[44] Wang, S. M.; Didziokas, M.; Roscian, M.; Evans, S.; Rouget, I.; Herrel, A.; Moazen, M.; Souquet, L. A comparative analysis of the puncturing abilities of cephalopod beak rostra using engineering tools. *Mar. Biol.* **2024**, *171*, 131.

[45] Zhao, H. T.; Wang, X.; Geng, Z. H.; Liang, N. X.; Li, Q.; Hu, X. M.; Wei, Z. W. Dual-function microneedle array for efficient photodynamic therapy with transdermal co-delivered light and photosensitizers. *Lab Chip* **2022**, *22*, 4521–4530.

[46] Hou, Y.; Chen, C.; Liu, K. M.; Tu, Y.; Zhang, L.; Li, Y. B. Preparation of PVA hydrogel with high-transparence and investigations of its transparent mechanism. *RSC Adv.* **2015**, *5*, 24023–24030.

[47] Yue, T. Q.; Lu, C. H.; Tang, K. L.; Qi, Q. K.; Lu, Z. Y.; Lee, L. Y.; Bloomfield-Gadêlha, H.; Rossiter, J. Embodying soft robots with octopus-inspired hierarchical suction intelligence. *Sci. Robot.* **2025**, *10*, eadr4264.

[48] Tramacere, F.; Pugno, N. M.; Kuba, M. J.; Mazzolai, B. Unveiling the morphology of the acetabulum in octopus suckers and its role in attachment. *Interface Focus* **2015**, *5*, 20140050.

[49] Baik, S.; Kim, D. W.; Park, Y.; Lee, T. J.; Ho Bhang, S.; Pang, C. A wet-tolerant adhesive patch inspired by protuberances in suction cups of octopi. *Nature* **2017**, *546*, 396–400.

[50] Wang, Z. Y.; Wu, V. H.; Allevato, M. M.; Gilardi, M.; He, Y. D.; Luis Callejas-Valera, J.; Vitale-Cross, L.; Martin, D.; Amornphimoltham, P.; McDermott, J. et al. Syngeneic animal models of tobacco-associated oral cancer reveal the activity of *in situ* anti-CTLA-4. *Nat. Commun.* **2019**, *10*, 5546.

[51] Zheng, D. W.; Deng, W. W.; Song, W. F.; Wu, C. C.; Liu, J.; Hong, S.; Zhuang, Z. N.; Cheng, H.; Sun, Z. J.; Zhang, X. Z. Biomaterial-mediated modulation of oral microbiota synergizes with PD-1 blockade in mice with oral squamous cell carcinoma. *Nat. Biomed. Eng.* **2022**, *6*, 32–43.

[52] Siegel, R. L.; Kratzer, T. B.; Giaquinto, A. N.; Sung, H.; Jemal, A. Cancer statistics, 2025. *CA Cancer J. Clin.* **2025**, *75*, 10–45.

[53] Galluzzi, L.; Guilbaud, E.; Schmidt, D.; Kroemer, G.; Marincola, F. M. Targeting immunogenic cell stress and death for cancer therapy. *Nat. Rev. Drug Discov.* **2024**, *23*, 445–460.

[54] Gerstberger, S.; Jiang, Q. W.; Ganesh, K. Metastasis. *Cell* **2023**, *186*, 1564–1579.

[55] Mahvi, D. A.; Liu, R.; Grinstaff, M. W.; Colson, Y. L.; Raut, C. P. Local cancer recurrence: The realities, challenges, and opportunities for new therapies. *CA Cancer J. Clin.* **2018**, *68*, 488–505.

[56] Carrera, P. M.; Kantarjian, H. M.; Blinder, V. S. The financial burden and distress of patients with cancer: Understanding and stepping-up action on the financial toxicity of cancer treatment. *CA Cancer J. Clin.* **2018**, *68*, 153–165.